Frozen lattice and absorptive model for high angle annular dark field scanning transmission electron microscopy : a comparison study in terms of integrated intensity and atomic column position measurement

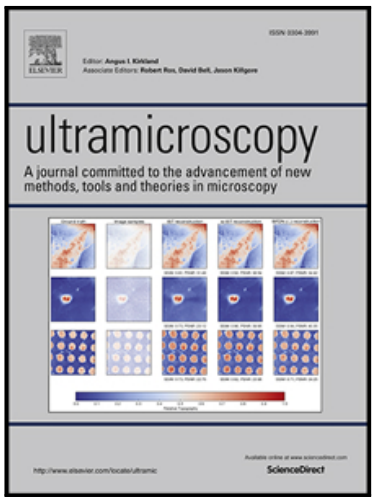

Frozen lattice and absorptive model for high angle annular dark field scanning transmission electron microscopy: a comparison study in terms of integrated intensity and atomic column position measurement

M. Alania, I. Lobato, S. Van Aert

PII: S0304-3991(17)30311-X
DOI: 10.1016/j.ultramic.2017.08.021
Reference: ULTRAM 12453

To appear in: *Ultramicroscopy*

Received date: 15 June 2017
Revised date: 25 August 2017
Accepted date: 29 August 2017

Please cite this article as: M. Alania, I. Lobato, S. Van Aert, Frozen lattice and absorptive model for high angle annular dark field scanning transmission electron microscopy: a comparison study in terms of integrated intensity and atomic column position measurement, *Ultramicroscopy* (2017), doi: 10.1016/j.ultramic.2017.08.021

Highlights

- STEM images are simulated using the frozen phonon and absorptive potential model.
- Both models are compared in a quantitative manner.
- A comparison is made in terms of integrated intensity and precision.
- For high angles and large thicknesses, the AP model underestimates the integrated intensity.
- Comparable results are predicted for the precision with which atomic columns can be located.

Frozen lattice and absorptive model for high angle annular dark field scanning transmission electron microscopy: a comparison study in terms of integrated intensity and atomic column position measurement

M. Alania, I. Lobato, S. Van Aert

Electron Microscopy for Materials Science (EMAT), University of Antwerp, Groenenborgerlaan 171, 2020 Antwerp, Belgium

Abstract

In this paper, both the frozen lattice (FL) and the absorptive potential (AP) approximation models are compared in terms of the integrated intensity and the precision with which atomic columns can be located from an image acquired using high angle annular dark field (HAADF) scanning transmission electron microscopy (STEM). The comparison is made for atoms of Cu, Ag, and Au. The integrated intensity is computed for both an isolated atomic column and an atomic column inside an FCC structure. The precision has been computed using the so-called Cramér-Rao Lower Bound (CRLB), which provides a theoretical lower bound on the variance with which parameters can be estimated. It is shown that the AP model results into accurate measurements for the integrated intensity only for small detector ranges under relatively low angles and for small thicknesses. In terms of the attainable precision, both methods show similar results indicating picometer range precision under realistic experimental conditions.

Keywords: Multislice simulations; Thermal diffuse scattering; Frozen phonon; Frozen lattice; Absorptive potential; STEM

1. Introduction

Material properties are strongly connected to the electronic structure, which in turn critically depend on the atom positions [1, 2]. It is well known that extremely small changes in the local atomic structure may result into significant changes in their properties [3, 4, 5]. Therefore, development of quantitative techniques to measure the atomic arrangement of projected atomic columns or individual atoms with sub-picometre precision is required. The enormous progress in aberration-corrected scanning transmission electron microscopy (STEM) makes it a powerful tool that enables structure characterisation and chemical mapping at the atomic scale with high precision [6, 7]. A key imaging mode is high angle annular dark field (HAADF) STEM, where the collected signal is sensitive to the structural and chemical composition.

Although modern STEM is capable of reaching sub-Angstrom resolution, quantitative structure determination requires accurate image simulations combined with statistical parameter estimation. The simulations are needed in order to understand the quantum mechanical nature of the

electron-specimen interaction, and statistical parameter estimation is needed in order to quantify or more correctly to estimate unknown structure parameters from STEM images. For high-angle scattering, the intensity is mainly dominated by Rutherford and thermal diffuse scattering (TDS). Therefore, most of the HAADF signal emitted by each atom contributes incoherently [8, 9]. This diffuse intensity, resulting from the phonon scattering, can be included in the multislice simulations by using realistic phonon calculations (frozen phonon) or by the Einstein model (frozen lattice (FL)). However, both models require repeated MS calculations for a large number of different configurations of the specimen. This process requires an enormous amount of computer calculations and is time-consuming, especially, for simulations involving high angle scattering where a dense sampling is required. As an alternative method, which is computationally less intensive and which requires only a single configuration for the specimen, the Absorptive Potential (AP) approximation model is often included into the MS algorithm [10, 11, 12, 13].

The main objective of this paper is to investigate to which extent the faster but less reliable absorptive model can tolerably be used to measure parameters from HAADF STEM images, which are often used to quantify the underlying structure. Therefore, in this paper, we will study the difference in intensities between the FL and the AP models for HAADF STEM images. First, we will compare the total integrated intensity scattered toward the annular STEM detector of an isolated atomic column and an atomic column inside an FCC structure. Next, the theoretical limit with which an atomic column can be located in two dimensions (2D) based on HAADF STEM images is explored. The calculation of the attainable precision is based on the concept of Fisher information and expresses a theoretical lower bound on the attainable variance. This study has been done for three different atom types, selected as a function of their scattering factor amplitude: weakly scattering atoms, e.g. copper (Cu); medium scattering atoms, e.g. silver (Ag); and strongly scattering atoms, e.g. gold (Au).

The organisation of this paper is as follow. In section 2, the electron-specimen interaction theory, the methods used to simulate STEM images, and the theory for computing the attainable precision are described. In section 3, the parameters used for the STEM simulations are summarised. In Section 4, the numerical results are discussed. Finally, in section 5, conclusions are drawn.

2. Theoretical background

STEM image simulations are based on a full quantum mechanical treatment of the dynamical scattering that occurs during electron propagation through the specimen [12]. It has been demonstrated that the non-relativistic Schrödinger equation with the relativistically correct mass and wavelength yields accurate results for typical energy ranges used in the transmission electron microscope [14, 15, 16, 17]. In the paraxial approximation, that is, parallel to the optical axis (z-axis), this equation may be written as [18]

$$\left[\Delta_{xy} + \frac{4\pi i}{\lambda}\frac{\partial}{\partial z} + \frac{2me}{\hbar^2}V(\mathbf{r})\right]\psi(\mathbf{r}) = 0 \tag{1}$$

where

$$V(\mathbf{r}) = \sum_i V_i(\mathbf{r} - \mathbf{r_i}) \tag{2}$$

is the electrostatic Coulomb potential, which is given by the sum of the electrostatic potentials of all atoms in the specimen. Furthermore, $\mathbf{r} = (x, y, z)$ is a set of three-dimensional (3D) Cartesian coordinates, $\hbar = h/2\pi$ is Planck's constant divided by 2π, $m = \gamma m_0$ is the relativistic mass of the electron, and Δ_{xy} is the Laplacian operator with respect to the x-, and y-axis coordinates. One of the most suitable approaches for the numerical calculation of the latter equation is the MS method [18].

2.1. Multislice method

The MS method developed by Cowley and Moodie [19], and later performed for fast computation by Ishizuka [11] and Rez [20] is one of the most efficient methods to solve the non-relativistic Schrödinger equation given by Eq. (1). In this method, the specimen potential is divided into many slices along the electron beam propagation. Each slice has to be thin enough to be considered as a weak phase object, which modifies only the phase of the incident wave. The potential between two consecutive slices is considered to be zero and the propagation of the electron wave within the slice is approximated by the Fresnel propagator, which involves a convolution in real space. The electron wave at any depth z_n can be calculated by repeated application of this process [11, 18]. The mathematical formalism of the multislice method can be expressed as

$$\psi_{n+1}(\mathbf{R}, z_{n+1}) = P(\mathbf{R}, \varepsilon) \otimes [T(\mathbf{R}, z_n)\psi_n(\mathbf{R}, z_n)] + \mathcal{O}(\varepsilon^2) \tag{3}$$

where $\mathbf{R} = (x, y)$ is the set of two-dimensional (2D) Cartesian coordinates and ε is the distance between the slices z_n and z_{n+1},

$$P(\mathbf{R}, \varepsilon) = \frac{1}{i\lambda\varepsilon} \exp\left(\frac{i\pi}{\lambda\varepsilon}(x^2 + y^2)\right) \tag{4}$$

is the Fresnel propagator, and

$$T(\mathbf{R}, z_n) = \exp\left(i\sigma \int_{z_n}^{z_n+\varepsilon} V(\mathbf{R}, z')dz'\right), \tag{5}$$

is the transmission function for the correspondent slice with $\sigma = 2\pi m\lambda/h^2$ the interaction parameter. The 2D convolution operator ($\otimes$) is defined as

$$f(\mathbf{R}) \otimes g(\mathbf{R}) = \int f(\mathbf{R}')g(\mathbf{R} - \mathbf{R}')d^2\mathbf{R}'. \tag{6}$$

2.2. Frozen phonon method

The low-intensity diffuse background in between the normal diffraction peaks is strongly related to the atomic vibration [21]. This background intensity that will be referred to as thermal diffuse scattering (TDS) produces effects in both diffraction patterns and ADF STEM images. In the standard multislice calculation, this effect is neglected [22]. The best way to describe TDS is by using the frozen phonon model [21, 23]. This model has been proved in a rigorous way to be fully equivalent to a full quantum mechanical treatment of the inelastic phonon scattering [24], and has been demonstrated to result in a good match with the experiment even for thicker specimens [25] and specimens containing heavy atoms [26]. This method is based on a basic classical description in which each electron sees a different configuration of atoms displaced from their

equilibrium positions. The resulting image intensity is obtained by averaging the simulated images performed for a certain number of configurations. The displacement of the atoms due to the vibration of the specimen can be calculated by molecular dynamics, DFT calculations, or using a random number generator with a Gaussian distribution which is the equivalent to the Einstein model (FL) of the density of states for phonons [18].

Assuming that the total specimen potential $V(\mathbf{r},t)$ and the electron wave $\psi(\mathbf{r},t)$ are time-dependent, these equations can be written as [24, 27]:

$$V(\mathbf{r},t) = \langle V(\mathbf{r})\rangle + W(\mathbf{r},t) \tag{7}$$

$$\psi(\mathbf{r},t) = \langle \psi(\mathbf{r})\rangle + \delta(\mathbf{r},t) \tag{8}$$

where $\langle\ \rangle$ is the average taken over time t. It is important to note that this should not necessarily refer to the real time. In general, it can refer to each state of the object. In repeated multislice calculations, it refers to a frozen phonon configuration. From Eqs. (7) and (8), it follows

$$\langle W(\mathbf{r},t)\rangle = 0, \tag{9}$$

$$\langle \delta(\mathbf{r},t)\rangle = 0. \tag{10}$$

Using these assumptions, Van Dyck [24] has shown that the frozen phonon model allows us to split the total intensity into a coherent and an incoherent contribution. By taking the square of Eq. (8) and using Eq. (10), the total intensity at depth z can be calculated as

$$\left\langle |\psi(\mathbf{R},z)|^2 \right\rangle = |\langle \psi(\mathbf{R},z)\rangle|^2 + \left\langle |\delta(\mathbf{R},z)|^2 \right\rangle \tag{11}$$

Note that the explicit time dependence has been dropped from here on in order to simplify the notation. The first term on the right-hand side corresponds to the coherent intensity (i.e. elastic scattering) and the second term corresponds to the incoherent intensity (i.e. inelastic scattering), respectively. This derivation also holds in Fourier space. Therefore, for each probe located at the position (x_k, y_l), the intensity can be calculated by integrating the total intensity (coherent plus incoherent) over the detector:

$$f_{kl} = \int_{detector} \left\langle |\Psi(\mathbf{g},z)|^2 \right\rangle d^2\mathbf{g}, \tag{12}$$

where $\mathbf{g} = (g_x, g_y)$ is a 2D vector in reciprocal space and $\Psi(\mathbf{g},z)$ is the Fourier transform of $\psi(\mathbf{R},z)$.

2.3. Absorptive potential method

The absorptive potential approximation [28, 11, 13], computed from e.g. the Weickenmeier and Kohl parametrization [29], is a quasi-coherent approach in which the distribution of the atomic displacements due to the thermal vibration of the atoms into the specimen is described by the convolution of the atomic scattering factors with a Gaussian function. The intensities of the STEM image are then calculated by using a modified, complex, projected potential $V(\mathbf{R})$ [11]:

$$V(\mathbf{R}) = V_r(\mathbf{R}) + iV_i(\mathbf{R}). \tag{13}$$

The diffuse intensity now results from the presence of an imaginary component $V_i(\mathbf{R})$, which is known as the absorptive potential. This potential is evaluated using the absorptive form factor defined in [30]. The real component, $V_r(\mathbf{R})$, corresponds to the normal electrostatic potential, which can be calculated using the elastic atomic scattering factors tabulated in [31]. Following [11], the total intensity can be calculated as the sum of both coherent and TDS contributions for each position of the probe (x_k, y_l):

$$f_{kl} = I_{kl}^{coherent} + I_{kl}^{TDS}. \tag{14}$$

The coherent contribution is described by

$$I_{kl}^{coherent} = \int_{detector} |\Psi(\mathbf{g}, z)|^2 d^2\mathbf{g}, \tag{15}$$

where $\Psi(\mathbf{g}, z)$ is the Fourier transform of $\psi(\mathbf{R}, z)$, which can be computed using the multislice method where the potential is given by the complex potential defined by Eq. (13). The incoherent contribution is given by

$$I_{kl}^{TDS} = \sum_{n=1}^{m} \int |\psi_n(\mathbf{R}, z_n)|^2 V_n^{TDS}(\mathbf{R}) d^2\mathbf{R}, \tag{16}$$

where m refers to the total number of slices, $\psi_n(\mathbf{R}, z_n)$ is given by Eq. (3) using the complex potential defined by Eq. (13), and $V_n^{TDS}(\mathbf{R})$ can be derived from the absorptive potential $V_i(\mathbf{R})$ following [11].

2.4. Statistical measurement precision

Ultimately, the precision with which unknown structure parameters can be estimated, such as the 2D positions of projected atom columns or 3D locations of individual atoms, is limited by noise. Indeed, due to noise, the pixel values that constitute the experimental images will fluctuate randomly from experiment to experiment. These pixel values, which we will from now on refer to as observations, can be modelled as random variables, characterized by a joint probability function (PF). In a STEM experiment, the observations are counting results, for which the PF can be modelled as a Poisson distribution. Based on the PF, an expression for the highest attainable precision with which structure parameters of the sample under study can be estimated in an unbiased way can be derived using the concept of Fisher information [32, 33]. This expression defines a lower bound on the variance of any unbiased estimator of a parameter and is known as the Cramér-Rao lower bound (CRLB). Consider a set of stochastic observations w_{kl}, $k = 1, ..., K$, $l = 1, ...L$. Then, the vector w defined as

$$w = (w_{11}, ..., w_{KL})^T \tag{17}$$

represents the column vector of these observations of dimension $K \times L$, where $K \times L$ corresponds to the dimension of each image. If the observations are assumed to be statistically independent, Poisson distributed variables, the probability that the observation w_{kl} is equal to ω_{kl} is given by [34]

$$\frac{\lambda_{kl}^{\omega_{kl}}}{\omega_{kl}!} exp(-\lambda_{kl}) \tag{18}$$

with λ_{kl} the expected number of detected electrons at pixel (k, l). The expected number of detected electrons per pixel position (k, l) equals

$$\lambda_{kl} = f_{kl}\frac{I\tau}{e} \tag{19}$$

with f_{kl} the fraction of electrons expected to be recorded by the detector, I the probe current in ampere, τ the recording dwell time for one pixel, and $e = 1.6 \times 10^{-19}$ C the electron charge. These expectation values can be simulated using either the FL model using Eq. (12) or the AP model using Eq. (14) within the MS algorithm. When assuming statistically independent observations, the probability $P(\omega;\beta)$ that a set of observations $w = (w_{11}, ..., w_{KL})^T$ is equal to $\omega = (\omega_{11}, ..., \omega_{KL})^T$ is the product of all the probabilities described by Eq.(18):

$$P(\omega;\beta) = \prod_{k=1}^{K}\prod_{l=1}^{L}\frac{(\lambda_{kl})^{\omega_{kl}}}{\omega_{kl}!}\exp\left(-\lambda_{kl}\right). \tag{20}$$

This function is the joint PF of the observations. Since the expectation values depend on the choice of the structure of the object under study, the unknown structure parameters β enter $P(\omega;\beta)$ via λ_{kl}. The expression for the joint PF enables one to compute the CRLB. The Fisher information matrix F for estimation of a set of unknown structure parameters β is defined as

$$F = -\mathbb{E}\left[\frac{\partial^2 \ln P(\omega;\beta)}{\partial\beta\partial\beta^T}\right] \tag{21}$$

where $\mathbb{E}[\ ]$ is the expectation operator. The expression between brackets is the Hessian matrix of $\ln P(\omega;\beta)$ of which the (p,q)th element is defined as

$$\frac{\partial^2 \ln P(\omega;\beta)}{\partial\beta_p\partial\beta_q} \tag{22}$$

where β_p and β_q correspond to the p and qth element of the vector β, respectively. The elements $F(p,q)$ may be calculated explicitly using Eqs.(19)-(22) [35]:

$$F(p,q) = \sum_{k=1}^{K}\sum_{l=1}^{L}\frac{1}{\lambda_{kl}}\frac{\partial\lambda_{kl}}{\partial\beta_p}\frac{\partial\lambda_{kl}}{\partial\beta_q}. \tag{23}$$

It is important to note that the dimension of the Fisher information matrix depends on the number of parameters to be estimated. Suppose that $\hat{\beta}$ is an unbiased estimator of β. The Cramér-Rao inequality then states that [36]

$$cov(\hat{\beta},\hat{\beta}) \geq F^{-1} \tag{24}$$

where $cov(\hat{\beta},\hat{\beta})$ is the variance-covariance matrix of the estimator $\hat{\beta}$, defined by its (p,q)th element $cov(\hat{\beta}_p,\hat{\beta}_q)$. Its diagonal elements are thus the variances of the elements of $\hat{\beta}$. The matrix F^{-1} is called the Cramér-Rao lower bound on the variance of $\hat{\beta}$. The Cramér-Rao inequality (24) expresses that the difference between the left-hand and right-hand member is positive semi-definite. A property of a semi-definite matrix is that its diagonal elements cannot be negative. This means that the diagonal elements of $cov(\hat{\beta},\hat{\beta})$ will always be larger than or equal to the corresponding diagonal elements of the inverse of the Fisher information matrix. Therefore, the diagonal elements of F^{-1} define lower bounds on the variances of the elements of $\hat{\beta}$

$$var(\hat{\beta}_p) \geq \sigma^2_{\hat{\beta}_p} = F^{-1}(p,p) \tag{25}$$

where $F^{-1}(p,p)$ is the (p,p)th element of the inverse of the Fisher information matrix.

3. Simulation settings

In this paper, simulations of STEM images with the inclusion of the FL model and the AP model are performed using the MULTEM [37, 38] and STEMsim [13, 39] programs, respectively. Although both programs show the same results for simulations with FL calculations using the Weickenmeier and Kohl parametrization [29], the advantage of MULTEM with respect to STEMsim is the computation time. Especially since MULTEM uses the graphical processor unit (GPU) instead of the central processor unit (CPU), it is more time-efficient for this type of calculations. Simulations have been performed for isolated atomic columns and FCC structures of Cu, Ag, and Au atoms with a lattice parameter of 3.615 Å, 4.0853 Å and 4.078 Å, respectively. For the isolated columns, the distance between atoms in the column is chosen equal to the lattice parameter of their respective FCC structure.

In order to study the annular dependence, simulations are performed for a detector covering the range from 40 to 160 mrad in steps of 2 mrad. Moreover, simulations are performed using three detectors as shown in table 1. In STEM image formation, the intensity of each pixel of the image is the result of the intensity produced by diffracted electrons over the detector plane and integrated over the detector geometry. In this study, simulations have been performed assuming symmetric and concentric annular detectors with an ideal detector sensitivity. The Debye-Waller factor for the three atom types has been calculated [40] at a temperature of 300 K and the defocus value has been adjusted to the Scherzer conditions. The other parameters are shown in table 1. For the FL simulations, 200 configurations have been computed using the Einstein model.

Table 1: Parameters for the MS simulations

Parameter	Symbol	Value
Annular detector 1	D_1 (mrad)	40-80
Annular detector 2	D_2 (mrad)	80-120
Annular detector 3	D_3 (mrad)	120-160
Debye-Waller factor Cu	(Å^2)	0.5747
Debye-Waller factor Ag	(Å^2)	0.7612
Debye-Waller factor Au	(Å^2)	0.7003
Acceleration voltage	(kV)	300
Defocus	(Å)	-14.03
FWHM of the source image	(Å)	0.8
Spherical aberration	C_S (mm)	0.001
Spherical aberration of 5th order	C_5 (mm)	0.0
Convergence angle	α_0 (mrad)	21.00
Numerical real space grid		1536×1536

4. Numerical results

In this section, both approximation methods used to include the TDS signal in STEM image simulations, that is, the FL and AP model, will be compared in terms of: a) *integrated intensity* and b) *precision* with which an atomic column can be located. These quantities are important

to determine the structure and chemical composition of the specimen when using STEM experiments.

4.1. Integrated intensity

In this section, both the FL and the AP models will be compared in terms of the integrated intensity that is produced by an atomic column. This integrated intensity corresponds to the so-called scattering cross section [41], which has been shown to be a good measure to count the number of atoms in an atomic column from a single STEM image [6, 42, 43, 44, 45]. It is defined as the total scattered intensity integrated over the scanned area. Furthermore, the scanned area will be selected in such a way that the atomic column will be placed in the centre in order to collect most of the scattered intensity [46, 47]. The integrated intensity is defined as

$$I_{int} = \sum_{k}^{K} \sum_{l}^{L} f_{kl} \Delta x \Delta y, \tag{26}$$

with f_{kl} the fraction of electrons expected to be recorded by the detector at pixel (k, l) in a 2D STEM image with $K \times L$ pixels. Furthermore, Δx and Δy is the pixel size along the x- and y-axis, respectively (usually $\Delta x = \Delta y$).

The total intensity, calculated with the FL model is obtained by averaging the intensity of different configurations given by equation (12). Here, the MS method treats the interaction between the electron and the rigorously displaced atoms as an elastic (coherent) scattering process in which the scattered wave still interferes with the unscattered wave [48]. On the other hand, the AP model describes the TDS intensity by including absorption in the dynamical equation of the electron diffraction using a complex lattice potential, and calculates this intensity following equation (14). In order to make a comparison between both methods, the integrated intensity for three atom types (Cu, Ag and Au) will be investigated in three different ways. In 4.1.1, we will analyse how both methods distribute the integrated intensity over the annular detectors as a function of thickness. Next, in 4.1.2, the integrated intensity will be quantified for three detector ranges of an isolated column. In 4.1.3, this procedure will be repeated to quantify the integrated intensity of a column inside an FCC structure.

4.1.1. Distribution over the annular detector

Using equation (26), the integrated intensity produced by an isolated atomic column has been calculated as a function of thickness. To perform the simulations, a super cell of length $30 \times 30 \times L_{at}$ is considered with L_{at} the number of atoms in the column times the interatomic distance. Therefore, STEM images have been simulated with a pixel size of 0.15 Å over a square region with a side length of 20 Å. The atomic column with thickness up to 20 nm was placed in the centre of the scanned region. The annular detector covers a range from 40 to 160 mrad in steps of 2 mrad. For low angles, we refer to the lower values of this range. For each ring (annular detector of 2 mrad wide), the integrated intensity was computed. In this manner, it can be investigated how both methods distribute the intensity over the annular detector for atoms with different scattering factors. The results of these distributions are shown in figure 1.

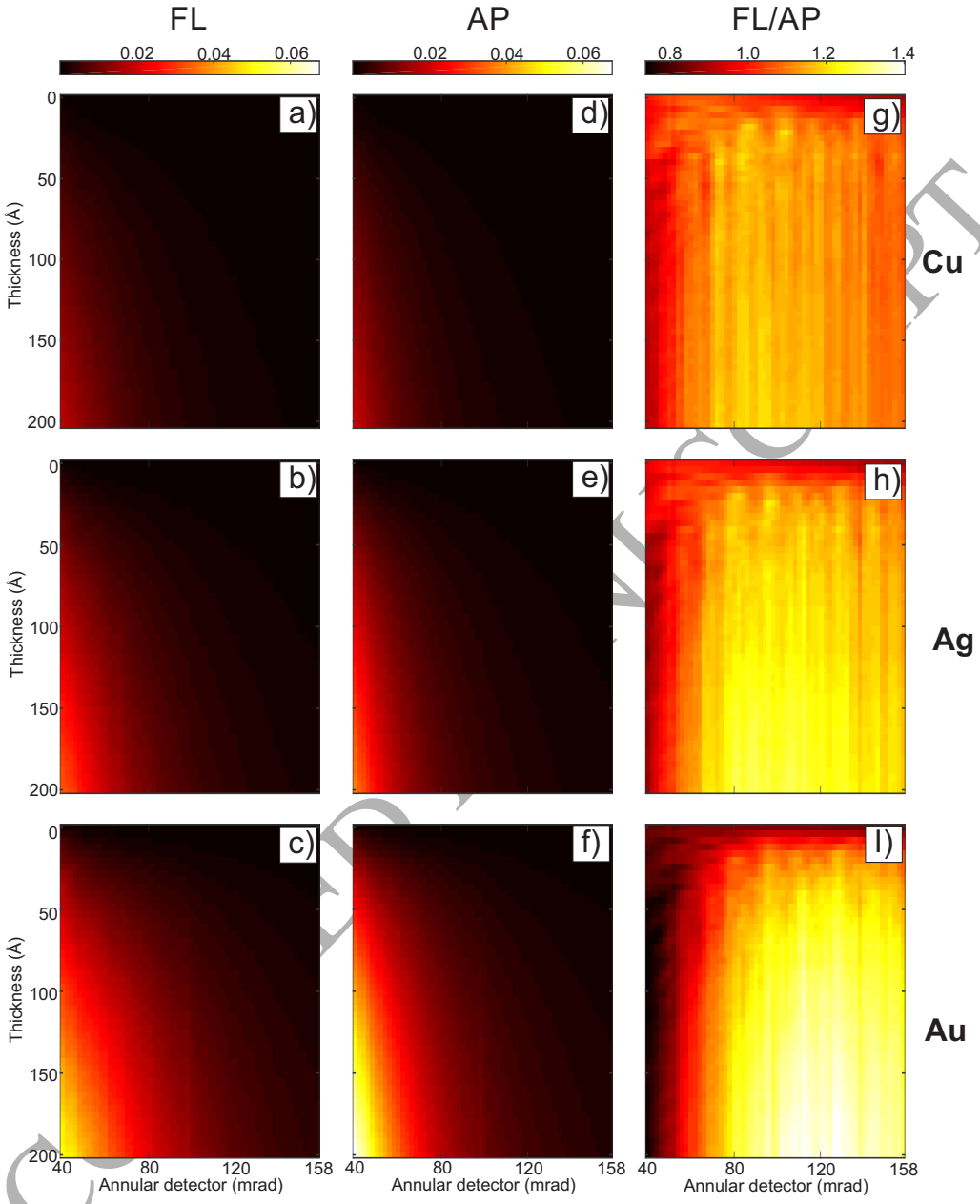

Figure 1: Distribution of the STEM integrated intensity over the detector range as a function of the thickness for an isolated column of atoms of Cu, Ag, and Au. The detector covering the range from 40 to 160 mrad was subdivided into 60 rings of 2 mrad each. The integrated intensity was calculated for each ring as a function of thickness. Figures a-c) show the results performed using the FL method. Figures d-f) show the results performed using the AP method. Figures g-i) show the proportion of the FL with respect to the AP method (FL/AP).

Figures 1a-c and 1d-f show the results of the distribution of the integrated intensity computed from simulations performed using the FL and the AP models, respectively. From these figures,

with equal scale-bar for the intensity, we can observe that the amount of intensity produced for both methods is different. The sensitivity of this difference between both methods may be a consequence of a break-down of the local approximation for the TDS absorption potential [49, 50] which suggests that the effect should be more pronounced in smaller detectors, in our case narrower detectors. This difference seems to change as a function of: a) thickness, b) detector range, and c) atom type. The ratio between intensities generated using both methods (FL/AP) is illustrated in figures 1g-i. For most detector angles and thickness values, the FL model results into higher intensities as compared to the AP model. Only for a small part of the detector range (low angles), the AP model has equal or higher intensity as compared to the FL model. These figures also demonstrate how the ratio between both methods depends on the atom type suggesting that this ratio increases as a function of the scattering factor. For example, the maximum ratio of the intensity for Au atoms (strong scattering factor) is larger as compared to the maximum ratio of intensities for atoms of Ag (medium scattering factor) and Cu (weak scattering factor).

More particularly, when comparing both methods for the three atoms types, we observe:

- *For atoms of Cu*: figures 1a,d show that both methods have a similar distribution of the scattered intensity. However, the ratio between both methods is not linear as we can see more clearly in figure 1e where larger differences between both methods are observed in the range between 70 to 120 mrad. For this atom type, the ratio between both models oscillates in the range from 0.9 to 1.2.

- *For atoms of Ag*: figures 1b,e show that the AP model produces more scattering than the FL model for low angles (lower than 50 mrad). For higher angles, the difference between both methods starts to increase, especially in the range from 80 to 120 mrad where the FL model results into higher intensities as compared to the AP model. This is shown in figure 1h. For this atom type, the ratio between both models oscillates in the range from 0.9 to 1.3.

- *For atoms of Au*: figures 1c,f show a similar behaviour for atoms of Ag although with even larger ratios between both methods. Figure 1i shows this behaviour more clearly. The largest difference between both methods is found in the range from 100 to 150 mrad and for thickness values larger than 100 Å. The ratio between both models oscillates in the range from 0.7 to 1.4. When comparing these results with the results shown in figures 1g and 1h, we can see that the detector range, where the AP model results into larger intensity values than the FL model increases as a function of scattering factor.

Based on this comparison, we can conclude that both models are only in good agreement in a very small detector range. This range depends on the atom type. Furthermore, the comparison shows that the AP model results into larger intensity values than the FL model for low angles. For larger angles, the FL model results into more scattering than the AP model. This distribution suggests that for detectors of realistic size, the integrated intensity depends on the collected detector range. For example, if we compute the integrated intensity for Au atoms using a detector ranging from 40 to 80 mrad, both methods will show similar results because the difference for low angles will be compensated with the difference observed for higher angles.

4.1.2. Integrated intensities for isolated columns

In the previous subsection, the distribution of the integrated intensity as a function of detector angle and thickness has been computed for both models. In order to quantify the difference of the

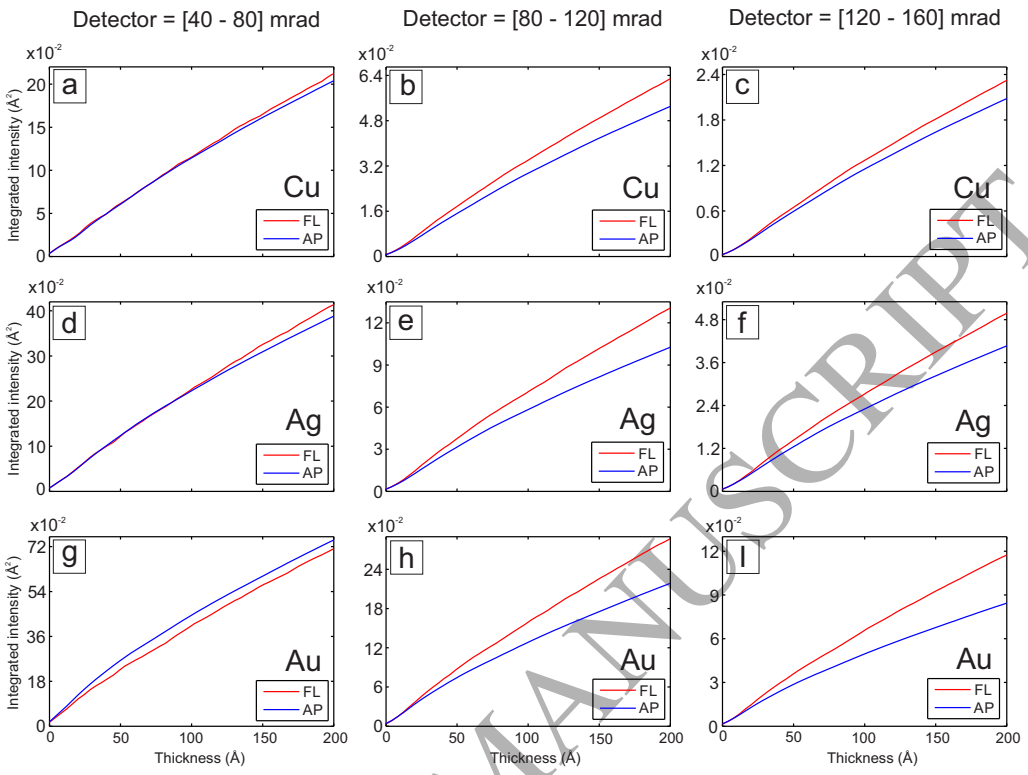

Figure 2: Integrated intensity as a function of thickness for an isolated column of atoms of Cu, Ag, and Au. The integrated intensity was calculated from simulations performed using the MS algorithm with the inclusion of the frozen phonon (red line) and absorptive potential (blue line). Figures a,d,g) correspond to the detector of 40 to 80 mrad; figures b,e,h) correspond to the detector of 80 to 120 mrad; and figures c,f,i) correspond to the detector of 120 to 160 mrad.

integrated intensity between both models for realistic detector settings, we proceed in the same way as in the previous subsection. We use the three detectors D_1, D_2, and D_3 defined in table 1 with all other parameters kept constant. The results are shown in figure 2, where the integrated intensity is plotted as a function of thickness for an atomic column consisting of Cu, Ag, and Au atoms. From these figures, we conclude that:

- for detector D_1 (first column of figure 2), both methods are in good agreement for small thicknesses with values around 140 Å, 100 Å, and 20 Å for atoms of Cu, Ag, and Au, respectively. For larger thicknesses, the FL model produces more intensity than the AP model for Cu and Ag, whereas for Au, the effect is opposite.

- for detector D_2 (second column of figure 2), both methods are in good agreement up to thicknesses around 20 Å for the three atom types. For larger thicknesses, the FL model produces more intensity than the AP model. The difference between both methods scales with the thickness and the scattering factor.

- for detector D_3 (third column of figure 2), both methods show the same behaviour as for detector D_2.

Assuming the FL as the most accurate model, we can conclude from the results shown in figure 2 that for detector D_1, the AP model underestimates the integrated intensity for Cu and Ag, whereas it overestimates for Au. Despite these differences, the fact that both methods show similar results for detector D_1 does not mean that both methods are distributing the intensity in the same way. This is shown in figures 1g-i. In this detector range, there is a compensation of the intensity. For angles close to 40 mrad, the AP model scatters more intensity and for angles close to 80 mrad the FL model scatters more intensity. For detectors D_2 and D_3, the AP model underestimates the intensity. This effect seems to increase as a function of thickness and also as a function of the scattering factor. A possible explanation for this observation can be found in the fact that the FL includes multiple elastic and TDS scattering to all orders [22] whereas the AP assumes that, once thermally scattered, the electrons are not scattered again [25].

The impact of the observed differences in intensity between both models will depend on the purpose for which the intensity is used. For example, if one wants to quantify the location of atomic columns from 2D STEM images, the difference in intensity between both methods is perhaps not important. However, if the analysis is focused on the quantification of the number of atoms or atom type, this difference can introduce wrong values. In equations (11) and (16), the intensity is related to the scattering factor amplitude of the atom type. From the results, we can observe that atoms with high scattering factor scatter more intensity to higher angles as compared to atoms with weak scattering factor. One should realize that this study is based on an isolated column and does not take into account the effect caused by cross-talk produced by the neighbouring columns [51, 52]. Therefore, in the next subsection we will analyse this effect for more realistic specimens.

4.1.3. Integrated intensities for FCC structures

To compare the integrated intensity between both models for more realistic specimens, where the cross-talk produced by neighbouring columns is taken into account, an FCC structure of Cu, Ag, and Au atoms with lattice parameters of 3.615 Å, 4.0853 Å, and 4.078Å, respectively, were assumed. The simulation were performed using a super cell of $36.1\times36.1\times L_{uc}$, $36.7\times36.7\times L_{uc}$ and $36.7\times36.7\times L_{uc}$ for atoms of Cu, Ag and Au, respectively, where L_{uc} is equal to the number of unit cells along the beam direction times the interatomic distance. We used the detectors D_1, D_2, and D_3, and the parameters mentioned in table 1. The integrated intensity was computed

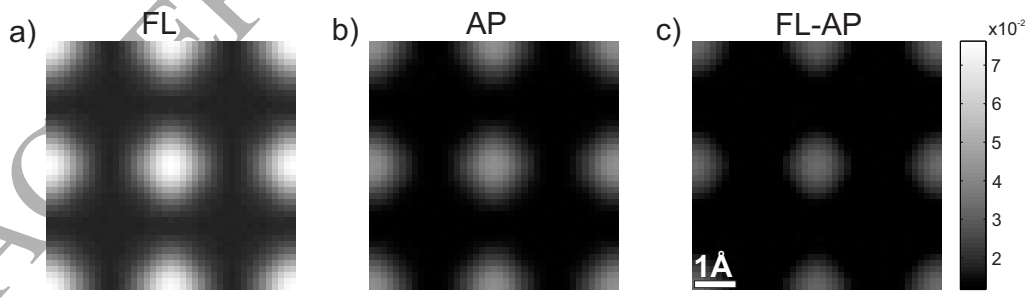

Figure 3: Simulated STEM images of an FCC structure of Au atoms along the [001] zone-axis for a thickness of 20 nm and a detector ranging from 120 to 160 mrad, using the MS algorithm with the inclusion of a) the frozen lattice model, and b) the absorptive potential approximation. Figure (c) is the difference between the frozen lattice and the absorptive potential approximation. All images are plotted on the same scale.

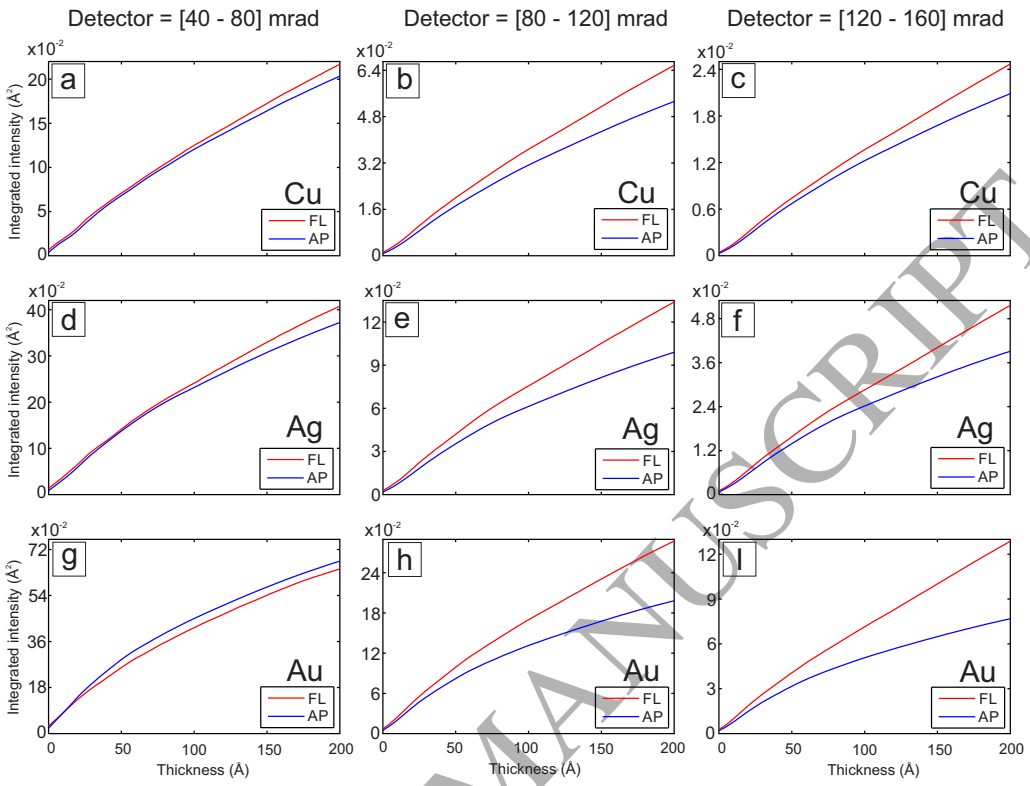

Figure 4: Integrated intensity as a function of thickness for an atomic column of an FCC structure of atoms of Cu, Ag, and Au. The integrated intensity was calculated from simulations performed using the MS algorithm with the inclusion of the FL (red line) and AP approximation (blue line). Figures a,d,g) correspond to the detector of 40 to 80 mrad; figures b,e,h) correspond to the detector of 80 to 120 mrad; and figures c,f,i) correspond to the detector of 120 to 160 mrad.

over a scanned area equivalent to one unit cell with a pixel size of 0.145 Å along the [001] zone-axis as shown in figure 3. In order to compare the integrated intensity with respect to one atomic column, the integrated intensity of one unit cell is divided by the number of projected atomic columns in one projected unit cell, which in this case equals 4. Using this criterion, the integrated intensity was computed as a function of thickness. The first, second and third column of figure 4 show the results of the integrated intensity as a function of thickness for the three atom types for detectors D_1, D_2 and D_3, respectively. When comparing these results with the integrated intensities computed for an isolated column, as shown in figure 2, only small differences are observed. In general the behaviour is the same for the three detectors and for the three atom types. Although neighbouring columns do not cause significant deviations in the integrated intensity, this effect depends on the detector range and thickness [53].

This study has also been performed for Au atoms with an acceleration voltage of 80 kV and 200 kV keeping the same input parameters and using the same equivalent semi-aperture angle and detectors used at 300 kV. At 80 kV, a semi-aperture angle of 44.5 mrad and equivalent detectors D_1, D_2, and D_3 of [84.9-170.3] mrad, [170.3-256.7] mrad and [256.7-344.7] mrad have been considered, respectively. At 200 kV, these values are equal to a semi-aperture angle of 26.7 mrad

and detectors of [50.9-101.9] mrad, [101.9-153.1] mrad and [153.1-204.3] mrad. The results at 80 kV and 200 kV are shown in figure 5. From this figure we can observe that at these lower voltages, both models show the same trend but the difference between both models increases as a function of thickness for the equivalent detector D_1. For detectors D_2 and D_3, the FL model has a steeper slope as compared to the AP model. For thicknesses up to about 10 nm, the intensities produced by the AP model are larger than those of the FL model. For larger thicknesses, the FL model results into larger intensities. Furthermore, the difference scales with thickness. As compared to the results obtained at 300 kV, larger differences are obtained at those lower acceleration voltages.

In general, the results of this section show that the AP model may lead to considerable differences as compared to the FL model. Especially for detectors D_2 and D_3, the intensity is underestimated as a function of thickness and atom type. Therefore, we need to be careful when using the AP model to quantify the number of atoms or atom type. It is also important to mention that this result cannot be generalized to all atom types. Table 2 shows the maximum difference in number of atoms between the FL and the AP model up to a thickness of 20 nm corresponding to 55 atoms of Cu and 49 atoms of Ag and Au in the column. Figure 4 shows that the AP model underestimates the number of atoms with respect to the FL model with only one exception for detector D_1, where the intensity is overestimated in the presence of Au atoms.

4.2. The ultimate precision

In this section, both the FL and AP models will be compared in terms of the ultimate precision with which an atomic column can be located in 2D from images acquired using HAADF

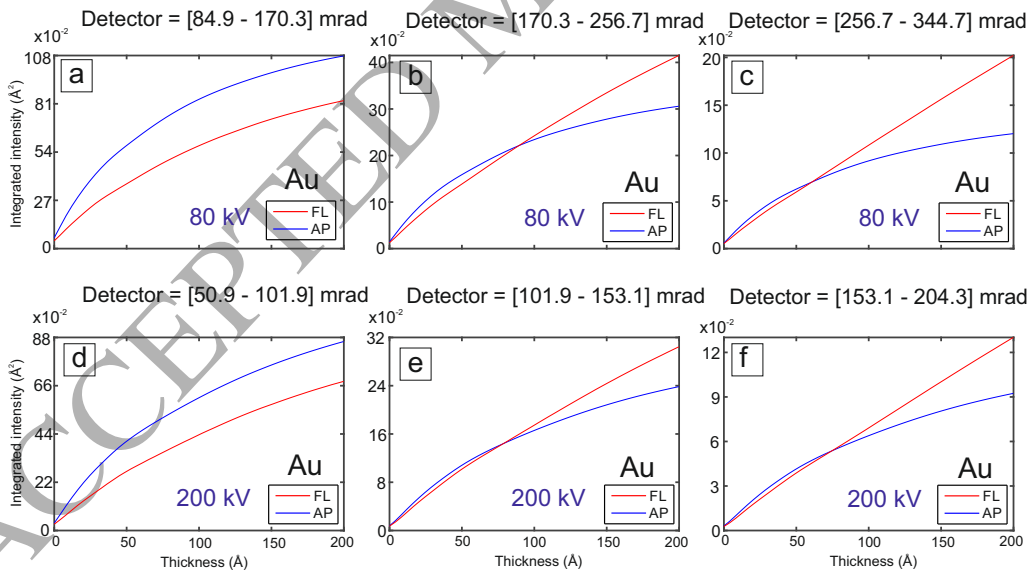

Figure 5: Integrated intensity as a function of thickness for an atomic column of an FCC structure of Au atoms. The integrated intensity was calculated from simulations performed using the MS algorithm with the inclusion of the FL model (red line) and the AP approximation (blue line). Figures a-c) correspond to an acceleration voltage of 80 kV with a detector range of [84.9-170.3] mrad, [170.3-256.7] mrad, and [256.7-344.7] mrad; figures e-g) correspond to an acceleration voltage of 200 kV with a detector range of [50.9-101.9] mrad, [101.9-153.1] mrad, and [153.1-204.3] mrad.

Table 2: Maximum difference in assigning the number of atoms when using the FL and AP model up to a thickness of 20 nm for each detector.

	D_1	D_2	D_3
Cu	4	12	10
Ag	5	14	14
Au	5	17	22

STEM [2, 54]. The ultimate precision, i.e. the lower bound on the standard deviation with which unknown structure parameters can be estimated unbiasedly, is given by the elements of the diagonal of the inverse of the Fisher information matrix F, defined by equation (23). From this equation, it is clear that the elements of the Fisher information matrix have to be calculated using the derivatives of the parametric model of the intensity observations λ_{kl} given by equation (19) with respect to the position coordinates of the projected atomic columns. In this study, the parametric model for the intensity observations λ_{kl} is simulated using the MS method.

As mentioned in section 2.1, the MS method is a numerical solution of the Schrödinger equation. In order to calculate the partial derivatives, additional sets of MS simulations are required in which a single atomic column is shifted along an axis. For example, for the derivative of an atomic column with respect to the x-coordinate, this column is displaced along the x-axis. The partial derivatives are then approximated using the following expression:

$$\lambda'(x) \approx \frac{\lambda(x+h) - \lambda(x)}{h} \tag{27}$$

where h is the shift of the column from its regular position along the x-axis. Similarly, the derivatives with respect to the y-axis can be calculated. The comparison between the FL and the AP models will be done in two ways. First, the ultimate precision to locate an isolated column of gold atoms from 2D STEM images is investigated. Next, the ultimate precision to locate a column inside an FCC structure is studied. For both cases, it will be investigated if the FL and AP models lead to the same results for the ultimate precision. For these calculations, the convergence of the derivatives given by equation (27) was analysed as a function of the displacement h, the number of configurations in the FL model, and the pixel size of the images. In this manner, optimal values were found with $h = 2$ pm, 200 FL configurations, and a pixel size of 0.35 Å.

4.2.1. Isolated column

From equation (23), it can be seen that the calculation of the Fisher information matrix requires the derivatives of the expectation model λ_{kl} with respect to the unknown parameters. In this case, the unknown parameters are the projected x and y coordinates of an isolated atomic column given by the vector

$$\boldsymbol{\beta} = (\beta_x, \beta_y). \tag{28}$$

Because of the cylindrical symmetry of the image intensity distribution of an atomic column, the derivatives with respect to the x- and y-axis are the same. Therefore, the Fisher information matrix simplifies to:

$$F = \begin{bmatrix} F_{11} & F_{12} \\ F_{12} & F_{22} \end{bmatrix}. \tag{29}$$

From equation (24) it follows that the CRLB on the variance, that is, $\sigma^2_{\beta_x}$ or $\sigma^2_{\beta_y}$, is given by the corresponding diagonal element of F^{-1}:

$$\sigma^2_{\beta_x} = \sigma^2_{\beta_y} = F^{-1}(1,1). \tag{30}$$

The square root of the values of equation (30) gives us a lower bound on the standard deviation $\sigma = \sigma_{\beta_x} = \sigma_{\beta_y}$.

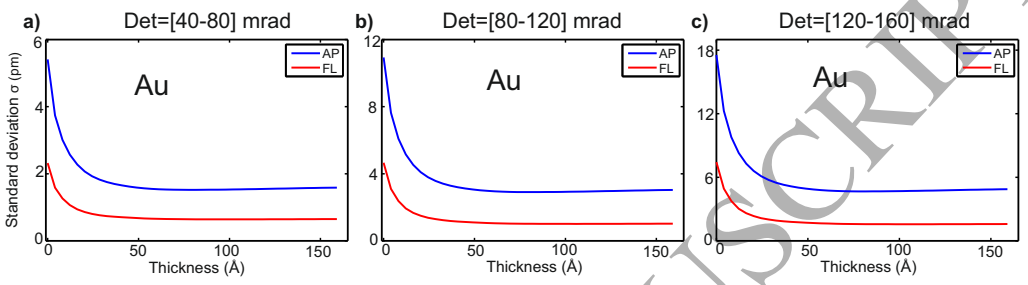

Figure 6: The ultimate precision σ to locate an isolated column of gold atoms as a function of thickness from simulated STEM images performed using the MS algorithm with the inclusion of the FL model (red line) and the AP model (blue line) for three detectors: a) [40-80] mrad, b) [80-120] mrad, and c)[120-160] mrad.

The CRLB has been computed for the FL and AP using a square region of 12.234 Å with a pixel size of 0.3398 Å for the atomic column at the centre of this region. An incident electron dose of 21652 $e^-/\text{Å}^2$ was used corresponding to a beam current of 40 pA and pixel dwell time $\tau = 10\mu$s. The results for the precision are shown in figure 6 as a function of thickness. From this figure we can observe that the ultimate precision has the same behaviour for both methods for the three detectors. The precision improves as a function of thickness but beyond a certain value the gain in precision is marginal. For higher angles, the precision decreases i.e. the standard deviation increases. However, when comparing the results of both methods, the FL model shows a better precision for the three detectors as compared to the AP model. The difference between both methods is approximately constant with thickness. It is important to note that the precision is different for both methods even for the detector D_1 where similar results for the integrated intensities were found. Figure 2(g) shows that the AP model scatters more intensity than the FL but in terms of precision the FL model predicts a better precision as shown in figure 6(a). The reason for this is that the distribution of the intensity over the scanned area is different for both methods.

4.2.2. FCC structure

In section 4.2.1, the ultimate precision to locate an atomic column in 2D was computed for an isolated column. In order to compute this theoretical limit on the precision for an atomic column where its intensity is affected by the cross-talk of the neighbouring columns, an FCC structure was assumed. The precision also depends on the atom types. Calculations were therefore performed for both the AP and the FL models using the same settings as for the integrated intensity in section 4.1.3.

Figure 7 shows the results of the ultimate precision as a function of thickness for the three atom types. From this figure, the precision with which a column of Cu atoms can be located

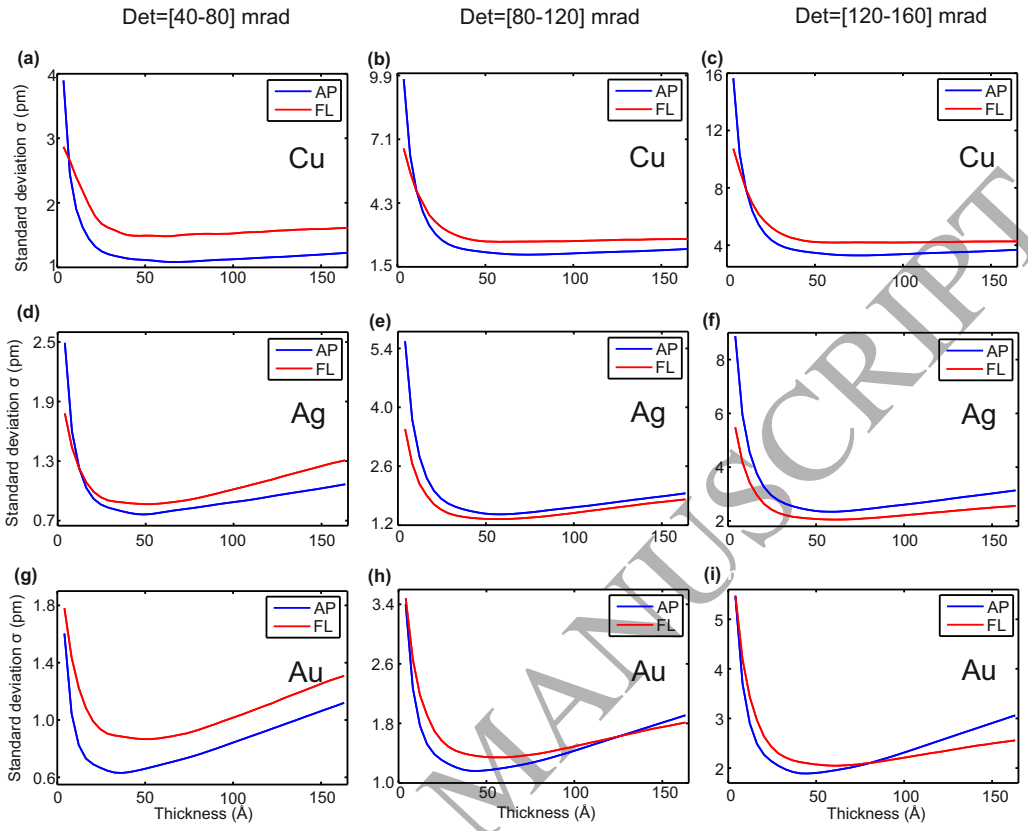

Figure 7: The ultimate precision to locate the central atomic column of Cu, Ag, and Au atoms in an FCC structure using the collected intensity of three detectors: a,d,g) [40-80] mrad. b,e,h) [80-120] mrad. c,f,i) [120-160] mrad. The precision was computed from simulated STEM images performed using the MS algorithm with the inclusion of the FL (red line) and AP approximation (blue line).

shows a similar behaviour for both methods. The precision improves as a function of thickness. However, beyond a certain value this gain is only marginal. For Ag and Au, the precision first improves as a function of thickness and beyond a certain value the precision starts to decrease. This behaviour is more pronounced for Au than for Ag. These results show that the behaviour of the ultimate precision to locate an atomic column from 2D STEM images for the three atom types is strongly related to their scattering factor amplitude. For atoms with a small scattering factor amplitude such as Cu, the intensity is scattered close to the location of the atomic column position and therefore the contribution due to crosstalk is small. For atoms with a medium scattering factor such as Ag, the effect of crosstalk starts to make an influence on the calculation of the precision. For atoms with a strong or high scattering factor amplitude, such as Au, the influence of crosstalk is even more pronounced in the calculation of the precision.

From figure 7, it may also be observed that the precision differs for both models. For atoms of Cu, the AP shows a better precision as compared to the FL model for thicknesses larger than 1 nm for the three detector ranges. This difference increases as a function of the angles, i.e.

detectors with higher angles result into a larger difference for the precision. For atoms of Ag, the same behaviour is presented for detector D_1. For detectors D_2 and D_3, the FL presents a better precision as compared to the AP model for all thicknesses. For atoms of Au, the behaviour of the precision for detector D_1 is the same as presented for atoms of Cu. For detectors D_2 and D_3, the AP shows a better precision for small thicknesses, and the FL for larger thicknesses. It is important to mention that the attainable precision with which atomic column positions can be measured, can be used to optimize the settings of the electron microscope [55, 56]. The observed differences between the predicted precision for both methods shown in figure 7 is small enough to accurately predict the optimal settings and to get an accurate prediction of the precision that can ultimately be attained.

5. Conclusions

In this work, two of the most popular methods used to simulate STEM images, the frozen phonon and the absorptive potential model, were compared in terms of the integrated intensity and the theoretical limits with which an atomic column can be located in 2D based on the acquisition of HAADF STEM images.

The integrated intensity was computed by integrating the total scattered intensity over the scanned area. The results show a similar trend of the intensity as a function of thickness but with different values for both models in the cases of an isolated atomic column and an atomic column within an FCC structure. For the detector ranging from 40 to 80 mrad the difference of the integrated intensity between both models is small especially for small thicknesses. For the detectors ranging from 80 to 120 mrad and from 120 to 160 mrad, this difference increases as a function of thickness and atom type. This means that atoms with a strong scattering factor results into a larger difference in the integrated intensity. From this comparison, the results suggest that we need to be careful when using the absorptive potential model for quantification when using the integrated intensity because for high angles and large thicknesses this model underestimates the integrated intensity.

Using the concept of the Cramér-Rao lower bound, the ultimate precision with which an atomic column can be located from 2D HAADF STEM images has been computed for an isolated column of Au atoms and for an atomic column within an FCC structure of Cu, Ag, and Au atoms. For an isolated atomic column of Au atoms, the precision improves as a function of thickness, but beyond a certain value, the gain in precision is marginal for both methods. However, for all thicknesses, the frozen phonon predicts a better precision as compared to the absorptive potential model. For the atomic column of an FCC structure, the ultimate precision depends on the atom type and detector range. For the detector ranging from 40 to 80 mrad, the absorptive potential shows a better precision with respect to the frozen phonon model for the three atom types. For the detectors ranging from 80 to 120 mrad, the results for both methods are similar. The difference between both methods are in the picometre scale for the simulation settings used in this paper.

Acknowledgements

The authors acknowledge financial support from the Research Foundation Flanders (FWO, Belgium) through project fundings (G.0374.13N, G.0369.15N,and G.0368.15N). A. Rosenauer is

acknowledged for providing the STEMsim program.

References

[1] D. Wolf, S. Yip, Materials Interfaces: Atomic-level Structure and Properties, Springer Netherlands, 1992. URL https://books.google.be/books?id=d7vi0rHqoLIC

[2] S. Van Aert, A. J. den Dekker, A. van den Bos, D. Van Dyck, High-resolution electron microscopy: from imaging toward measuring, IEEE Transactions on Instrumentation and Measurement, 51 (4).

[3] Y. Tang, Y. Zhu, Y. Wang, W. Wang, Y. Xu, W. Ren, Z. Zhang, X. Ma, Atomic-scale mapping of dipole frustration at 90 charged domain walls in ferroelectric PbTiO3 films, Scientific reports 4.

[4] T. Qi, I. Grinberg, A. M. Rappe, Correlations between tetragonality, polarization, and ionic displacement in PbTiO3-derived ferroelectric perovskite solid solutions, Physical Review B 82 (13) (2010) 134113.

[5] N. Alem, O. V. Yazyev, C. Kisielowski, P. Denes, U. Dahmen, P. Hartel, M. Haider, M. Bischoff, B. Jiang, S. G. Louie, et al., Probing the out-of-plane distortion of single point defects in atomically thin hexagonal boron nitride at the picometer scale, Physical review letters 106 (12) (2011) 126102.

[6] S. Van Aert, J. Verbeeck, R. Erni, S. Bals, M. Luysberg, D. Van Dyck, G. Van Tendeloo, Quantitative atomic resolution mapping using high-angle annular dark field scanning transmission electron microscopy, Ultramicroscopy 109 (10) (2009) 1236–1244.

[7] T. Grieb, K. Müller, R. Fritz, V. Grillo, M. Schowalter, K. Volz, A. Rosenauer, Quantitative chemical evaluation of dilute GaNAs using ADF STEM: Avoiding surface strain induced artifacts, Ultramicroscopy 129 (2013) 1–9.

[8] R. F. Loane, P. Xu, J. Silcox, Incoherent imaging of zone axis crystals with ADF STEM, Ultramicroscopy 40 (2) (1992) 121–138.

[9] P. Hartel, H. Rose, C. Dinges, Conditions and reasons for incoherent imaging in STEM, Ultramicroscopy 63 (2) (1996) 93–114.

[10] K. Watanabe, T. Yamazaki, I. Hashimoto, M. Shiojiri, Atomic-resolution annular dark-field STEM image calculations, Physical Review B 64 (11) (2001) 115432.

[11] K. Ishizuka, A practical approach for STEM image simulation based on the FFT multislice method, Ultramicroscopy 90 (2) (2002) 71–83.

[12] M. Croitoru, D. Van Dyck, S. Van Aert, S. Bals, J. Verbeeck, An efficient way of including thermal diffuse scattering in simulation of scanning transmission electron microscopic images, Ultramicroscopy 106 (10) (2006) 933–940.

[13] A. Rosenauer, M. Schowalter, J. T. Titantah, D. Lamoen, An emission-potential multislice approximation to simulate thermal diffuse scattering in high-resolution transmission electron microscopy, Ultramicroscopy 108 (12) (2008) 1504–1513.

[14] K. Fujiwara, Relativistic dynamical theory of electron diffraction, Journal of the Physical Society of Japan.

[15] H. Ferwerda, B. Hoendersa, C. Slumpa, Fully relativistic treatment of electron-optical image formation based on the Dirac equation, Optica Acta 33 (1986) 145–157.

[16] R. Jagannathan, Quantum theory of electron lenses based on the Dirac equation, Physical Review A 42 (11) (1990) 6674.

[17] R. Jagannathan, R. Simon, E. Sudarshan, N. Mukunda, Quantum theory of magnetic electron lenses based on the Dirac equation, Physics Letters A 134 (8) (1989) 457–464.

[18] J. Kirkland, Advanced Computing in Electron Microscopy, SpringerLink: Springer e-Books, Springer US, 2010. URL https://books.google.be/books?id=YscLlyaiNvoC

[19] J. M. Cowley, A. F. Moodie, The scattering of electrons by atoms and crystals. I. A new theoretical approach, Acta Crystallographica 10 (10) (1957) 609–619.

[20] P. Rez, The use of array processors attached to minicomputers for multislice image calculations, Ultramicroscopy 16 (2) (1985) 255–259.

[21] D. A. Muller, B. Edwards, E. J. Kirkland, J. Silcox, Simulation of thermal diffuse scattering including a detailed phonon dispersion curve, Ultramicroscopy 86 (3) (2001) 371–380.

[22] R. F. Loane, P. Xu, J. Silcox, Thermal vibrations in convergent-beam electron diffraction, Acta Crystallographica Section A: Foundations of Crystallography 47 (3) (1991) 267–278.

[23] Z. Wang, The frozen-lattice'approach for incoherent phonon excitation in electron scattering. How accurate is it?, Acta Crystallographica Section A: Foundations of Crystallography 54 (4) (1998) 460–467.

[24] D. Van Dyck, Is the frozen phonon model adequate to describe inelastic phonon scattering?, Ultramicroscopy 109 (6) (2009) 677–682.

[25] J. M. LeBeau, S. D. Findlay, L. J. Allen, S. Stemmer, Quantitative atomic resolution scanning transmission electron microscopy, Physical Review Letters 100 (20) (2008) 206101.

[26] J. M. LeBeau, A. J. DAlfonso, S. D. Findlay, S. Stemmer, L. J. Allen, Quantitative comparisons of contrast in

experimental and simulated bright-field scanning transmission electron microscopy images, Physical Review B 80 (17) (2009) 174106.
[27] S. Takagi, On the temperature diffuse scattering of electrons I. Derivation of general formulae, Journal of the Physical Society of Japan 13 (3) (1958) 278–286.
[28] S. Pennycook, D. Jesson, High-resolution Z-contrast imaging of crystals, Ultramicroscopy 37 (1-4) (1991) 14–38.
[29] A. Weickenmeier, H. Kohl, Computation of absorptive form factors for high-energy electron diffraction, Acta Crystallographica Section A: Foundations of Crystallography 47 (5) (1991) 590–597.
[30] C. Hall, P. Hirsch, Effect of thermal diffuse scattering on propagation of high energy electrons through crystals, in: Proceedings of the Royal Society of London A: Mathematical, Physical and Engineering Sciences, Vol. 286, The Royal Society, 1965, pp. 158–177.
[31] J. Ibers, W. Hamilton, International Tables for X-ray Crystallography: Vol. 4, Revised and supplementary tables to volumes II and III, no. v. 2; v. 4, Kynoch Press, 1974.
URL https://books.google.be/books?id=EllBmwEACAAJ
[32] A. van den Bos, A. J. den Dekker, Resolution reconsidered - Conventional approaches and an alternative, Advances in Imaging and Electron Physics 117 (2001) 241–360, San Diego: Academic Press. doi:10.1016/S1076-5670(01)80114-2.
[33] A. J. den Dekker, S. Van Aert, A. van den Bos, D. Van Dyck, Maximum likelihood estimation of structure parameters from high resolution electron microscopy images. Part I: A theoretical framework, Ultramicroscopy 104 (2) (2005) 83 – 106.
[34] D. C. Boes, F. A. Graybill, M. Alexander, Mood, Introduction to the theory of statistics (1974).
[35] S. Van Aert, A. den Dekker, D. Van Dyck, A. van den Bos, Optimal experimental design of STEM measurement of atom column positions, Ultramicroscopy 90 (4) (2002) 273–289.
[36] M. G. Kendall, The advanced theory of statistics. Vol. II (1947).
[37] I. Lobato, D. Van Dyck, MULTEM: A new multislice program to perform accurate and fast electron diffraction and imaging simulations using Graphics Processing Units with CUDA, Ultramicroscopy 156 (2015) 9–17.
[38] I. Lobato, S. Van Aert, J. Verbeeck, Progress and new advances in simulating electron microscopy datasets using MULTEM, Ultramicroscopy.
[39] A. Rosenauer, M. Schowalter, STEMSIM a new software tool for simulation of STEM HAADF Z-contrast imaging, in: Microscopy of Semiconducting Materials 2007, Springer, 2008, pp. 170–172.
[40] H. Gao, L.-M. Peng, Parameterization of the temperature dependence of the Debye–Waller factors, Acta Crystallographica Section A: Foundations of Crystallography 55 (5) (1999) 926–932.
[41] A. De Backer, G. Martinez, K. MacArthur, L. Jones, A. Béché, P. Nellist, S. Van Aert, Dose limited reliability of quantitative annular dark field scanning transmission electron microscopy for nano-particle atom-counting, Ultramicroscopy 151 (2015) 56–61.
[42] M. Retsky, Observed single atom elastic cross sections in a scanning electron microscope, Tech. rep., Chicago Univ., Ill.(USA). Dept. of Physics (1974).
[43] A. Singhal, J. Yang, J. Gibson, STEM-based mass spectroscopy of supported Re clusters, Ultramicroscopy 67 (1-4) (1997) 191–206.
[44] S. Van Aert, A. De Backer, G. Martinez, B. Goris, S. Bals, G. Van Tendeloo, A. Rosenauer, Procedure to count atoms with trustworthy single-atom sensitivity, Physical Review B 87 (6) (2013) 064107.
[45] A. De Backer, G. Martinez, A. Rosenauer, S. Van Aert, Atom counting in HAADF STEM using a statistical model-based approach: methodology, possibilities, and inherent limitations, Ultramicroscopy 134 (2013) 23–33.
[46] K. E. MacArthur, L. B. Jones, P. D. Nellist, How flat is your detector? Non-uniform annular detector sensitivity in STEM quantification, Journal of Physics: Conference Series 522 (1) (2014) 012018.
URL http://stacks.iop.org/1742-6596/522/i=1/a=012018
[47] A. Rosenauer, K. Gries, K. Müller, A. Pretorius, M. Schowalter, A. Avramescu, K. Engl, S. Lutgen, Measurement of specimen thickness and composition in AlxGa1-xN/GaN using high-angle annular dark field images, Ultramicroscopy 109 (9) (2009) 1171–1182.
[48] D. Van Dyck, Persistent misconceptions about incoherence in electron microscopy, Ultramicroscopy 111 (7) (2011) 894–900.
[49] C. Rossouw, L. Allen, S. Findlay, M. Oxley, Channelling effects in atomic resolution stem, Ultramicroscopy 96 (3) (2003) 299–312.
[50] M. Ohtsuka, T. Yamazaki, Y. Kotaka, H. Fujisawa, M. Shimizu, K. Honda, I. Hashimoto, K. Watanabe, Nonlocality in spherical-aberration-corrected haadf stem images, Acta Crystallographica Section A: Foundations of Crystallography 69 (3) (2013) 289–296.
[51] R. F. Loane, P. Xu, J. Silcox, Incoherent imaging of zone axis crystals with ADF STEM, Ultramicroscopy 40 (2) (1992) 121–138.
[52] D. O. Klenov, S. Stemmer, Contributions to the contrast in experimental high-angle annular dark-field images, Ultramicroscopy 106 (10) (2006) 889–901.

[53] G. T. Martinez, A. Rosenauer, A. De Backer, J. Verbeeck, S. Van Aert, Quantitative composition determination at the atomic level using model-based high-angle annular dark field scanning transmission electron microscopy, Ultramicroscopy 137 (2014) 12–19.

[54] J. Gonnissen, A. De Backer, A. den Dekker, J. Sijbers, S. Van Aert, Detecting and locating light atoms from high-resolution STEM images: The quest for a single optimal design, Ultramicroscopy 170 (2016) 128–138.

[55] M. Alania, A. De Backer, I. Lobato, F. Krause, D. Van Dyck, A. Rosenauer, S. Van Aert, How precise can atoms of a nanocluster be located in 3d using a tilt series of scanning transmission electron microscopy images?, Ultramicroscopy 181 (2017) 134–143.

[56] M. Alania, T. Altantzis, A. De Backer, I. Lobato, S. Bals, S. Van Aert, Depth sectioning combined with atom-counting in haadf stem to retrieve the 3d atomic structure, Ultramicroscopy 177 (2017) 36–42.